Study on Catalysts and Bipolar Plates in Proton Exchange Membrane Fuel Cells for enhancing properties

Jiawei Wen [1,†], Xiang Gao [2,*,†], Yu Fu [3,†]

[1] Zijin School of Geology and Mining Fuzhou University, Fuzhou University, Fuzhou, 350108

[2] School of materials science and engineering, Jilin University, Changchun, China, 130022

[3] College of Materials and Chemistry, China Jiliang University, Hangzhou, China, 310018

*Corresponding author: gaoxiang1622@mails.jlu.edu.cn

[†] These authors contributed equally.

Abstract. Currently, proton exchange membrane fuel cells are a highly efficient clean energy conversion technology, and their performance optimisation depends on the synergistic innovation of catalysts and bipolar plates. This paper systematically studies strategies for enhancing the activity of non-platinum catalysts and the synergistic optimisation mechanism of bipolar plate flow field and materials. The design of atomically dispersed Fe-N-C sites, heteroatom doping, and the construction of porous carbon carriers to create high-density active centres significantly enhance the kinetics of the oxygen reduction reaction. The Fe-N-C system can achieve a half-wave potential of 0.78–0.92 V in acidic media, and its peak power density is 890 mW/cm², approaching the level of commercial Pt/C. The new square baffle channel and symmetrical serpentine flow field can increase power density by 12.1–22.9%, while the metal foam structure reduces reactant consumption by 30%. CrAlCN and TiZrC coatings reduce interfacial contact resistance to 1.60 mΩ·cm², achieve corrosion current density at the 10^{-8} A·cm^{-2} level, and attain a water contact angle of 121.7°±1.0°. Research indicates that regulating the electronic state of non-platinum catalyst active sites and optimising mass transfer and electrical conductivity in bipolar plates are important to overcoming performance bottlenecks in PEMFCs, providing theoretical support and engineering pathways for low-platinum fuel cell technology.

Keywords: PEMFC, Non-platinum catalysts, Bipolar plate optimization, Flow field configuration.

1. Introduction

With the intensification of the traditional fossil fuel crisis and issues of the environmental pollution, the development of efficient and clean proton exchange membrane fuel cells (PEMFC) has become an significant direction for energy transition [1, 2]. It features high energy conversion efficiency, clean and pollution-free reactions, low operating temperatures, making it a highly efficient, clean, and renewable energy utilisation method [3, 4].

The chemical energy of hydrogen can be directly converted into electrical energy by PEMFCs through electrochemical reactions [5-7]. Hydrogen is dissociated into protons and electrons under the action of a catalyst at the anode. The protons pass to the cathode through the proton exchange membrane, and the electrons can form a current through the external circuit. At the cathode, oxygen combines with protons and electrons to form water, achieving zero pollution emissions. Electrode materials serve as the core carriers of electrochemical reactions and must simultaneously perform the functions of gas diffusion, electron conduction, and proton transport at the three-phase interface [8]. Their porosity, conductivity, and chemical stability directly affect the mass transfer efficiency of reactants and the rate of charge transfer [9]. The catalyst significantly improves the reaction kinetics by lowering the activation energy of the hydrogen oxidation reaction (HOR) and oxygen reduction reaction (ORR).

However, its application still has some shortcomings, such as the insufficient activity, and poor durability [10]. Traditional platinum catalysts have high precious metal loading and are prone to agglomeration and deactivation, resulting in delayed battery reaction kinetics and efficiency degradation [11, 12]. Issues such as carbon carrier corrosion and uneven distribution of polymers in

the electrode material can damage the integrity of the three-phase interface, exacerbating catalyst deactivation and proton conduction resistance [13, 14]. In addition, defects in the bipolar plate flow field design further exacerbate water-heat management imbalances and gas transport resistance. In response to these challenges, the synergistic optimisation of bipolar plates and catalysts has become key to improving the overall performance of PEMFCs.

This study addresses critical limitations in current PEMFC technology, where high-cost platinum-based catalysts suffer from insufficient activity, rapid degradation, and poor stability under operational conditions, while conventional bipolar plates often lead to inefficient mass transfer, high interfacial resistance, and inadequate water management. Existing non-platinum catalysts typically exhibit unsatisfactory oxygen reduction reaction kinetics with half-wave potentials below 0.75 V in acidic media and significant performance decay after fewer than 5,000 cycles, alongside limited power densities often under 600 mW/cm². Meanwhile, traditional flow field designs result in uneven gas distribution and considerable reactant waste, with corrosion current densities exceeding 10^{-6} A·cm^{-2} and contact resistance above 10 mΩ·cm². To overcome these barriers, this work focuses on the synergistic mechanism between atomically dispersed Fe–N–C catalysts with sulfur/selenium doping and optimized bipolar plate structures including symmetric serpentine flow fields and metal foam architectures. By simultaneously enhancing the intrinsic catalytic activity and improving mass transfer efficiency, this integrated strategy significantly advances cell performance and durability, offering a viable pathway to reduce reliance on precious metals and improve the economic feasibility of hydrogen energy systems.

2. Structure, and Properties of Catalysts

Catalysts are the core part of PEMFCs. Traditional platinum catalysts are severely limited in efficiency and cost-effectiveness due to their high cost, scarcity, and deactivation issues. So, developing high-activity, high-stability, low-cost non-platinum catalysts is key to breaking through efficiency bottlenecks, reducing system costs, and achieving the sustainable development of PEMFCs.

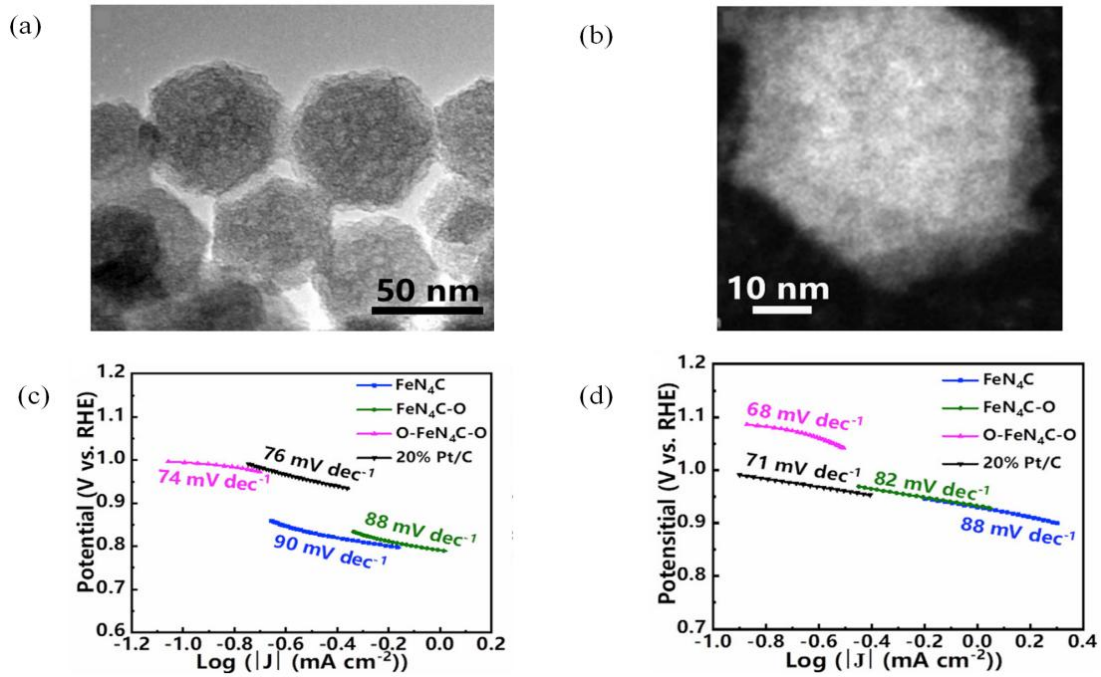

Figure 1. (a) TEM image of O-FeN$_4$C-O; (b) STEM image of O-FeN$_4$C-O; (c) Tafel plots in acidic condition; (d) Tafel plots of FeN$_4$C, O-FeN$_4$C, and O-FeN$_4$C-O and 20% Pt/C in alkaline solution [15].

Sun et al. investigated the synthesis, structure, and electrocatalytic performance of double oxygen-doped Fe–N–C single-atom catalysts (O-FeN$_4$C-O) [15]. The catalyst exhibits a polyhedral

morphology with no Fe agglomeration, as shown in Fig1 (a) and Fig1 (b). EDS analysis revealed uniform distribution of Fe, N, and O, with a BET surface area as high as 1461 m^2/g and pore sizes concentrated between 30–60 nm, demonstrating excellent mass transfer capability. XPS analysis showed an oxygen content of 7.68 at%, higher than the control group. O-FeN_4C-O exhibits ORR half-wave potentials of 0.78 V and 0.90 V in 0.5 M H_2SO_4 and alkaline electrolytes, respectively; The Tafel slope is as low as 74 mV/dec and 68 mV/dec, outperforming Pt/C and the control group, as shown in Fig1 (c) and Fig1 (d). After 10,000 cycles, the voltage decay is only 10–14 mV, with a current retention rate of 92.1%. DFT simulations indicate that axial and second shell (SCS) oxygen doping synergistically optimise the Fe–N_4 electron distribution, enhancing the binding energy between OH and OOH. D-band centre theory reveals an increase in the energy level of the Fe 3d orbital, enhancing adsorption and electron transfer capabilities. Axial Fe–O and SCS oxygen doping synergistically regulate electrons to improve reaction kinetics and stability. The multi-level pore structure and high specific surface area optimise mass transfer. Atomic-level Fe–N_4–O sites combine activity and stability, providing a new pathway for low noble metal-dependent PEMFC/AEMFC catalytic systems.

Cui et al. investigated trace Co-doped Fe-N-C single-atom catalysts Fe(tCo)-N-C [16]. The material exhibits a dodecahedral morphology as shown in Fig2 (a). It has a particle size of approximately 400 nm. Fe and Co atoms are uniformly dispersed without agglomeration, as shown in Fig2 (b), with a Fe/Co atomic ratio of 25.9 and a BET surface area of 1486 m^2/g. The formation of Fe_2N_8 coordination was confirmed, with a Fe–N coordination number of 3.8 and a bond length of 2.01 Å. Its half-wave potential in acidic and alkaline media reached 0.80 V and 0.89 V, respectively, outperforming Pt/C and Fe–N–C. The peak power density under H_2–O_2 conditions reaches 890 mW/cm^2, and under H_2–air conditions reaches 380 mW/cm^2; at a constant voltage of 0.5 V, 89% retention is maintained after 60 hours, with H_2O_2 production below 4% and an electron transfer number n ≈ 4, demonstrating excellent selectivity and stability, as shown in Fig2 (c) and Fig2 (d). DFT simulations indicate that the formation of *OH has a free energy barrier of only 0.51 eV, superior to the 0.63 eV of FeN_4. Trace Co doping induces the Fe_2N_8 structure and enhances graphitisation, while porous carbon improves reactant transport and conductivity, making it crucial for the catalyst's ORR activity, durability, and high-power output in PEMFCs.

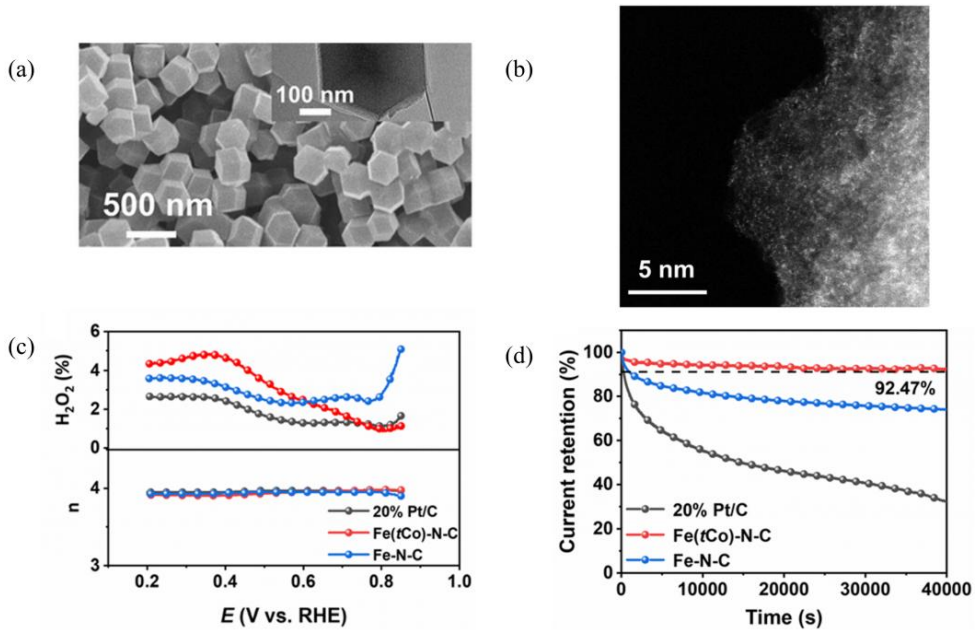

Figure 2. (a) Electron microscopy images of the catalysts; (b) AC HAADF scanning transmission; (c) The production of H_2O_2 and the electron transfer numbers; (d) CA at 0.7 V (1600 rpm) (O_2-saturated 0.1 M$HClO_4$) [16].

Akula et al. synthesised three commercial-grade Fe–N–C electrocatalysts using the VariPore™ process, retaining atomic-level Fe–N_x sites through a combination of high-temperature pyrolysis and acid washing strategies [17]. They are all porous carbon nanosheets with particle sizes ranging from 270 to 520 nm and surface areas of 640 to 725 m^2/g, as shown in Fig3 (a). XRD and Raman spectroscopy confirm moderate graphitisation and abundant defects, ID/IG ≈ 1, as shown in Fig3 (b). XPS indicates that N is primarily present in pyridine-, pyrrole-, and graphitic forms, as shown in Fig3 (c–e). In 0.5 M H_2SO_4, the ORR activity of the three materials is similar to that of Pt/C, with C30 performing the best, with $E_{1/2}$ = 0.76 V, Tafel slope 88 mV/dec, and electron transfer number≈3.98; after 10,000 cycles, $E_{1/2}$ decreases by only 30 mV, indicating that C30 is more stable than the other two. The catalytic mechanism is based on the synergistic effect of atomic-level Fe–N_x and N-doped structures, and the lone pair electrons of pyridine N polarise the O=O bond. Then, the graphite structure and mesoporous connectivity enhance reactant transport and charge transfer, thereby improving reaction kinetics. The VariPore™ process controls pore size and graphitisation degree to achieve highly dispersed active sites exposed on the carbon framework surface, preventing metal agglomeration, and forming a good mesoporous structure and low-resistance conductive network.

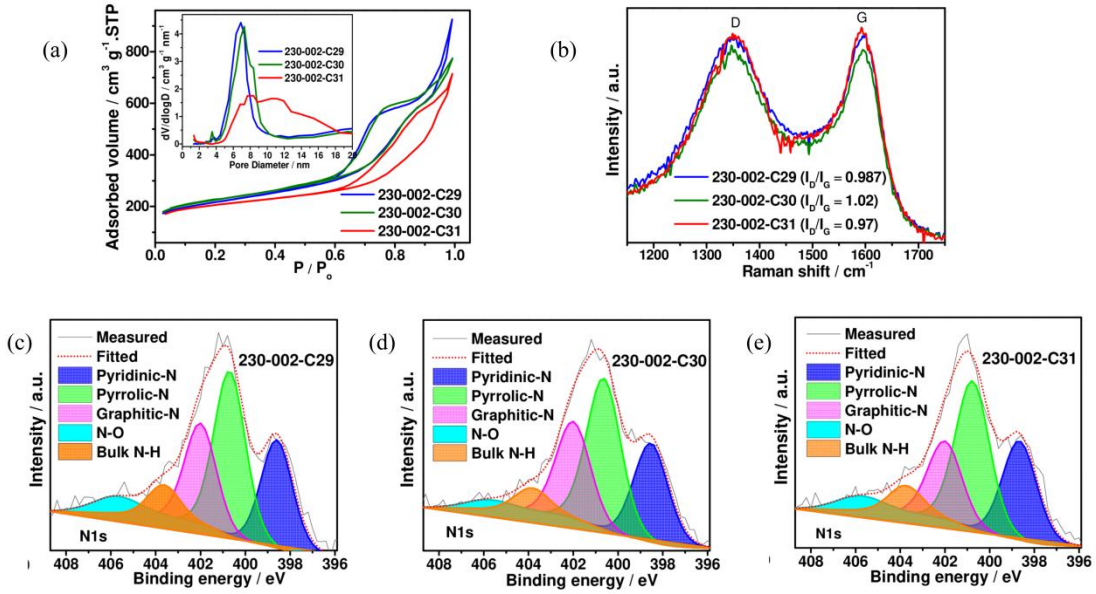

Figure 3. (a) Physisorption isotherms of N_2 and pore size distribution (inset); (b) Raman spectra of Fe–N–C catalysts. (c, d, e) N1s deconvoluted spectra of Fe-N-C catalysts [17].

Tao et al. focused on the construction strategies, catalytic mechanisms, and performance correlations of single-metal and bimetallic sites [18]. They combined PDA charge adsorption, acid leaching, NH_4Cl treatment, and other strategies to improve the dispersion and specific surface area of single atoms. The authors systematically categorised the structures of single-metal (Fe-N_4, Co-N_4, Co-N_3C) and bimetallic sites (e.g., $FeCoN_5$, Co_2N_5) and confirmed the existence of atomically dispersed metal sites using techniques such as EXAFS, AC HAADF-STEM, and XPS. The FeN_4S_2 structure exhibits a double-coordination structure with a primary shell of 4N and a secondary shell of 2S, as shown in Fig4 (a). And the Co_2N_5 binuclear site has a distance of 2.1 Å, confirming the coordination structure. Finally, various non-platinum catalysts demonstrate excellent activity, with CoSA-N-C (Co-N_3C site) exhibiting $E_{1/2}$ = 0.79 V; the CoN_{2+2} site in Fe-N-C@F127 exhibits $E_{1/2}$ = 0.84 V. N,S co-doped FeSA/NSC has a BET surface area as high as 1224 m^2/g, effectively exposing active sites, as shown in Fig4 (b). Additionally, the $Co_3(HADQ)_2$ two-dimensional conjugated MOF catalyst exhibits a half-wave potential of 0.825 V and excellent durability in acidic conditions, as shown in Fig4 (c). The article highlights the electronic regulation of processes such as O_2 adsorption and OOH dissociation by sites like Fe-N_4 and Co-N_3C. DFT calculations show that the activation energy for the rate-determining step at the Co-N_3C site is only 0.63 eV, significantly lower than the 0.94 eV at the Co-N_4 site. The Co_2N_5 site breaks the volcano curve limitation by synergistically

adsorbing *OOH/*O to regulate the electronic configuration. The synergistic interaction between high specific surface area, uniform M–N_x coordination centres, and secondary coordination (e.g., S, P) determines catalytic performance. For instance, auxiliary structures such as FeN_4P_2 and FeN_4S_2 enhance activity, and NH_4Cl treatment exposes more Fe–N_x sites and removes non-active metal particles to improve performance, as shown in Fig4 (d), providing theoretical and practical guidance for the development of efficient ORR catalysts.

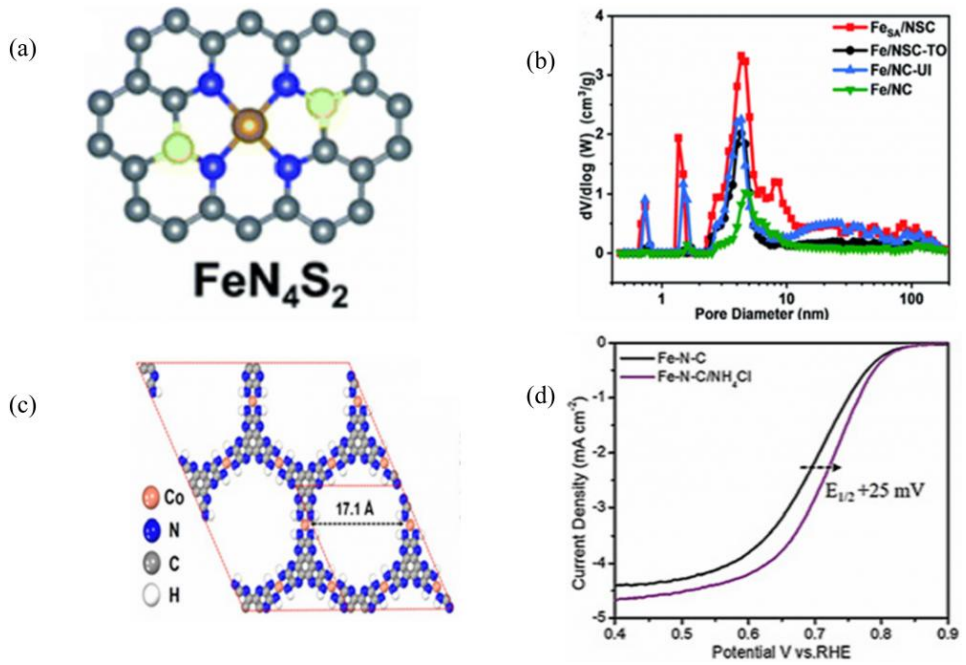

Figure 4. (a) Model of FeN_4S_2; (b) Pore size distribution curves of FeSA/NSC and other catalysts; (c) The structure of $Co_3(HADQ)_2$; ORR polarization plots of (d) The pristine and NH4Cl-treated Fe-N-C [18].

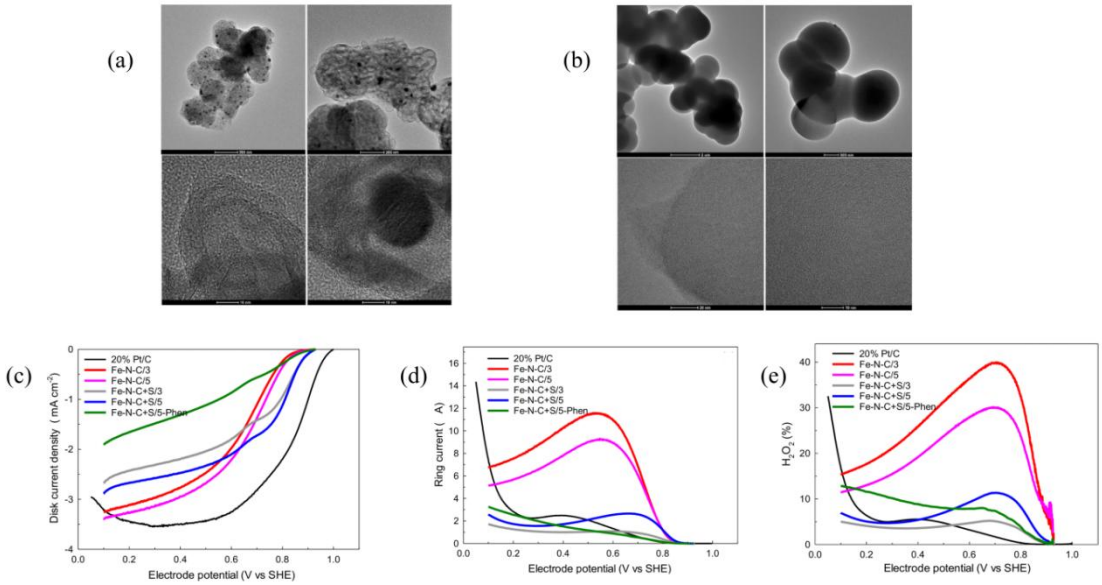

Figure 5. (a) TEM images of the S-free Fe-N-C/5; (b) TEM images of the S-doped Fe-N-C+S/5 materials; (c) Corrected disk currents; (d) Corresponding limiting ring currents; (e) Corresponding fraction of H_2O_2 formation during O_2 reduction calculated [19].

Kiciński et al. constructed Fe-N-C non-precious metal catalysts derived from nitrogen/sulphur co-doped polymers using the sol–gel method [19]. Structurally, it exhibits high graphitisation, low specific surface area (~280-290 m²/g), and a structure dominated by large pores. It features disordered carbon frameworks with a maximum specific surface area of 1020 m²/g and are rich in micropores.

XRD and Raman spectroscopy indicate that S-free materials contain Fe_3C/Feα nanoparticles, while iron in S-doped materials exists as single-atom Fe-N_x. TEM/EDS confirmed the morphological and distribution differences between the two, as shown in Fig5 (a) and Fig5 (b). S-doped materials, such as Fe-N-C+S/5, exhibit higher E_{onset}>0.85 V and $E_{1/2}$>0.78 V in RRDE testing, as shown in Fig5 (c-e). In PEMFC testing, the peak power density reached 0.15 W/cm². The enhanced catalytic activity stems from S doping regulating the spin state of Fe centres, enhancing microporous oxygen adsorption and cleavage, and facilitating charge transfer at surface functional groups. Although the structural differences among different samples are significant, their battery performance is comparable.

Baek et al. discovered a sulfur-doped porous carbon catalyst, S-CoNPC, derived from a bimetallic ZIF framework [20]. Structural characterisation revealed that S-CoNPC exhibits a polymeric polyhedral structure as shown in Fig6 (a). It has an average particle size of approximately 40 nm. It contains C, O, N, S, and Co elements, with a Co content of 1.52% (consistent with single-atom dispersion characteristics). HR-TEM and SAED analysis indicated an amorphous structure with numerous defects and highly conductive graphitised carbon, as shown in Fig6 (b) and Fig6 (c). Acid etching treatment increased the Co-Nx ratio and optimised the electronic structure. S-CoNPC exhibits excellent ORR performance under alkaline conditions: the onset potential E_{onset} = 0.906 V, the half-wave potential $E_{1/2}$ = 0.845 V, and the limiting current density is 6.67 mA/cm². The number of electron transfers is approximately 4, enabling efficient catalysis of ORR via a 4-electron pathway, as shown in Fig6 (d) and Fig6 (e). Its durability is remarkable, with a current retention rate of 99.4% after 10,000 cycles. Catalytic mechanism analysis indicates that its outstanding performance stems from the synergistic interaction between Co-Nx and C-S. The coupling of Co's d orbitals with O_2's 2p orbitals weakens the O-O bond, promoting O_2 dissociation. S's high electronegativity interacts with N's lone pair electrons to form new active sites, enhancing conductivity and surface activity. The structure-performance relationship shows that S doping and acid etching synergistically enhance specific surface area, defect site density, and electron transport capability, enabling Co-Nx sites to be fully exposed and efficiently catalyse ORR. Additionally, the formation of mesopores due to Zn volatilisation enhances mass transfer rates. Sulphur atoms weaken the adsorption strength of Co-Nx towards *OOH through electronic induction.

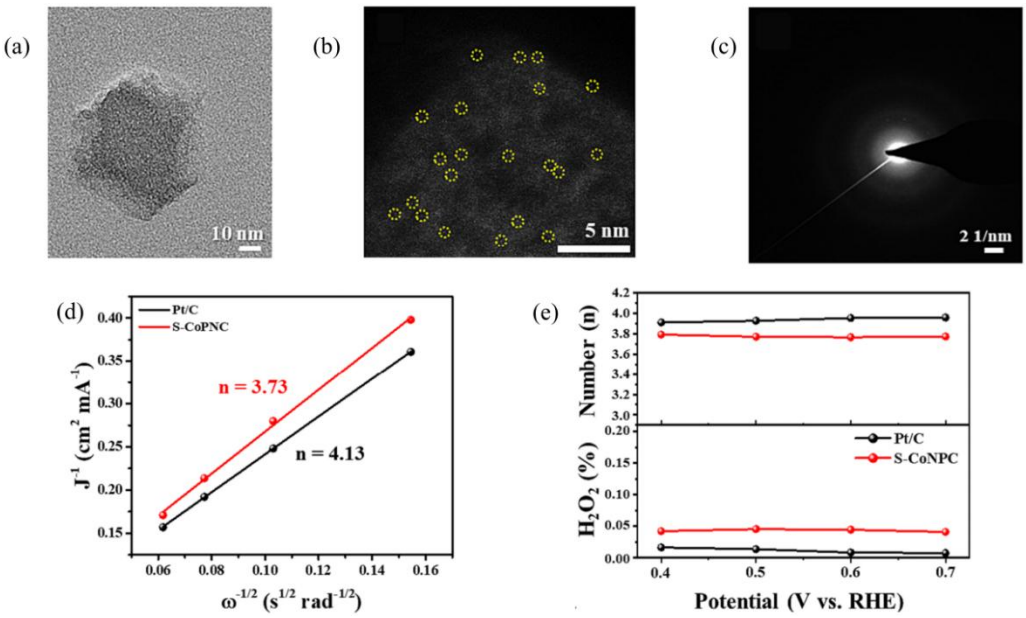

Figure 6. (a) SEM images of BMZIF; (b) HRTEM image of S-CoNPC in HAADAF mode; (c) SAED pattern of S-CoNPC. Electron transfer number plot obtained using (d) RDE and (e) RRDE with the %H_2O_2 [20].

Catalyst optimization in PEMFCs hinges on atomic site engineering, heteroatom coordination, and hierarchical porosity design. Atomically dispersed M-N_x sites such as Fe-N_4 and Co-N_3C significantly

reduce ORR activation energy, enabling half-wave potentials of 0.76 to 0.92 V in acidic electrolytes and peak power densities up to 890 mW/cm². Secondary coordination shells modified with heteroatoms like sulfur or phosphorus enhance electron transfer kinetics and oxygen adsorption, evidenced by DFT simulations revealing energy barriers as low as 0.51 eV for critical reaction steps. Hierarchical porous carbon carriers with BET surface areas ranging from 640 to 1486 m²/g and mesopore-dominated structures improve mass transfer efficiency while maintaining voltage decay within 30 mV after 10,000 cycles. In line with these advances, durability metrics across the surveyed non-Pt systems typically show ~10-30 mV voltage decay after 10,000 cycles, current retention of 89-99.4%, and H_2O_2 yields < 4% (n ≈ 4), indicating robust stability alongside maintained selectivity. However, persistent challenges include acid-induced dissolution of heteroatomic dopants exemplified by S-CoNPC performance degradation, mass transport resistance from thick catalyst layers of 50 to 70 μm, and inherent trade-offs between high activity sites like low-barrier Co-N_3C and their susceptibility to oxidative degradation.

3. Structure and Properties of Bipolar plates

The bipolar plate is the core component of the PEMFC. It can separate single cells, optimize mass transfer, and support the electrolytic cells. The materials primarily consist of metal and carbon-based composites, characterized by high electrical conductivity, corrosion resistance, and sufficient mechanical strength. The surface of metal bipolar plates is often treated with precious metal coatings, nitride/carbide coatings, and other coatings to reduce contact resistance and improve corrosion resistance.

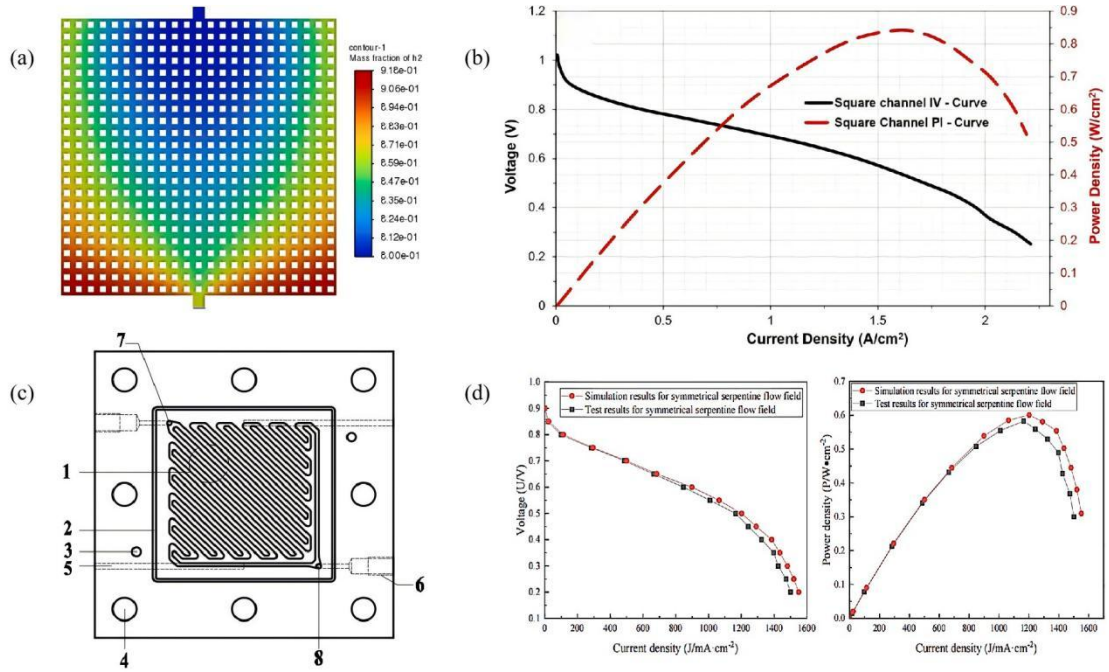

Figure 7. (a) The flow distribution for the square baffled channel; (b) Polarization curve for the square baffled channel [21]; (c) Schematic geometrical diagram for the new SSFF bipolar plate; (d) The test results of polarization curve and power density curve [22].

Tabbi Wilberforce et al. concluded that fuel cell property depends heavily on the geometry of the flow channels, as flow channels and stress concentration points directly impact cell pressure drop and mass transfer [21]. They can affect cell water management and thermal management, ultimately affecting cell property. They investigated the geometric design of novel bipolar plates, including a square baffled channel, a rectangular baffled channel, a parallel channel baffle, and a double serpentine channel design. Compared to other shapes, the square baffled channel has approximately 22.6% higher hydrogen mass fraction in water, as shown in Fig. 7(a). There is also better water

distribution to ensure ideal water management, reducing ohmic losses due to the ionic resistance of the membrane electrodes. The current density and power density are also higher, as shown in Fig. 7(b). The current density increased by 14.54%, 22.278%, and 67.72%, and the power density increased by 12.11%, 18.941%, and 77.88%. Yanqiang Wei et al. proposed a new symmetric serpentine flow field (SSFF) compared with the conventional serpentine flow field (CSFF) with a bipolar plate, as shown in Fig. 7(c) [22]. The SSFF structure enhanced the gas transfer between the channels. It also facilitated the discharge of product water, resulting in a more uniform distribution of water and oxygen between the gas diffusion layer and the catalyst layer. After simulation and electrochemical property test, the SSFF exhibited better electrochemical property, with a 22.9% increase in the fuel cell's maximum power density, as shown in Fig. 7(d).

Tabbi Wilberforce et al. investigated the effect of the material and structure of bipolar plates on their properties [23]. The PEM fuel cell with open-pore cellular foam (OPCF) was designed as shown in Fig. 8(a). The effect of inlet hydrogen pressure 1.5, 2.0 and 2.5 bar is considered and there is about 4-7% reduction of hydrogen consumption for OPCF and the reduction of air consumption is 4%. The OPCF can reduce reactant consumption and improve fuel cell efficiency. For consuming the same mass of fuel, the aluminium OPCF can work for a longer period, and it can also reduce the overall weight of the fuel cell. As shown in Fig. 8(b), aluminium flow plate material adsorbs reactants better and consumes an equal amount of hydrogen to produce a larger current. Longfei Liao et al. designed a new structure, shown in Fig. 8(c), consisting of a PTFE frame, sealing pads, a Ti mesh, and a flat Ti alloy plate to replace traditional bipolar plates [24]. The complex three-dimensional flow field is introduced by the embossed structure, and it is favorable for gas/water transfer and effectively improves the gas removal efficiency. At a current density of 1 A/cm^2, the electrolysis voltage of an embossed Ti mesh (1.844 V) was significantly lower than that of a flat Ti mesh (2.442 V), indicating that it can optimize reactant distribution and improve the efficiency of gas removal. The Platinum of 0.3 μm thickness further reduced the electrolysis voltage to 1.776 V, as shown in Fig. 8(d).

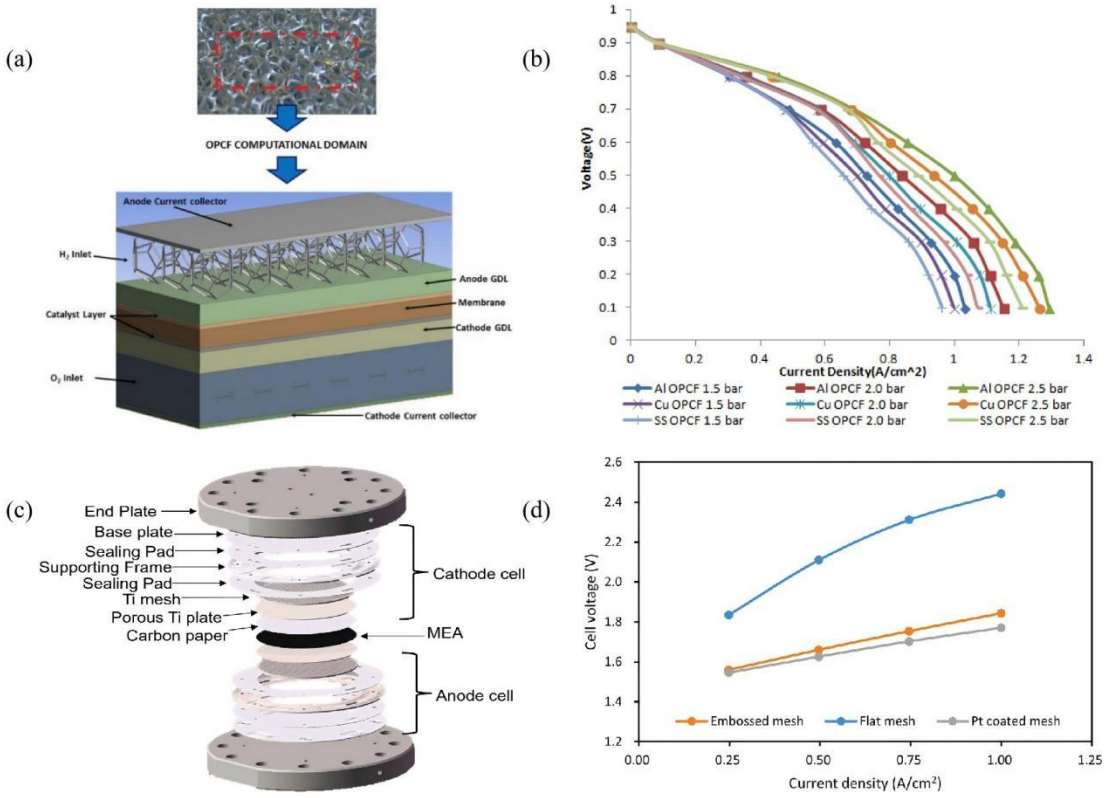

Figure 8. (a) PEM fuel cell with open pore cellular foam material; (b) Effect of different operating pressure at different polarization curve [23]; (c) The novel structure of the PEM electrolyzer; (d) Polarization curves obtained using a single-cell PEM electrolyzer with Ti mesh based bipolar plate [24].

Jie J et al. prepared CrAlCN quaternary coatings on the surface of SS316L stainless steel bipolar plates with different contents of carbon by the Closed Field Unbalanced Magnetron Sputter Ion Plating (CFUMSIP) technique to enhance their corrosion resistance, electrical conductivity, and hydrophobicity in PEMFC [25]. The coatings consisted of CrN, Cr_7C_7, AlN, and a small amount of oxides. The proportion of carbide Cr_7C_3 increased significantly with increasing carbon content (C_2H_2 flux from 0sccm to 12sccm). The test results showed that the C-8sccm coating sample as depicted in Fig. 9(a) exhibited a dense and uniform microstructure, with the lowest corrosion current density, indicating good corrosion resistance. The open-circuit voltage is 0.89 V. The maximum power density is 50.7 mW/cm^2. The C-8sccm coating had the largest water contact angle of 121.7° ± 1.0°, as shown in Fig. 9(b), and thus had the best hydrophobicity. The spherical particles protruding from the surface reduce the water droplet contact area, and it is favorable for water drainage in PEMFC. Tiancai Ma et al. prepared TiC and TiZrC coatings on 316L stainless steel substrates using Magnetron Sputter and Arc Ion Plating techniques to enhance their corrosion resistance, conductivity, and durability [26]. The TiZrC-coating showed the lowest surface roughness and achieved the highest hydrophobicity with an angle of 96.6°. The uncoated SS316L resulted a contact angle of 70.5°, and the TiC coating is 80.1°, exhibiting the hydrophilic nature. The interfacial contact resistance of the TiZrC coatings (1.60 mΩ·cm^2) was lower than that of the uncoated substrate (446 mΩ·cm^2) and the TiC coatings (2.33 mΩ·cm^2), as shown in Fig. 9(c). The TiZrC coatings were corroded by constant potentiostatic polarization for 100 h at 0.6 V. The corrosion resistance was also higher than the resistance of the uncoated substrate (446 mΩ·cm^2), and the TiC coatings were more resistant to corrosion. With constant potential polarization, the corrosion current density remained stable at 1.344 × 10-8 A·cm^{-2}, as shown in Fig. 9(d), indicating its long-term corrosion resistance.

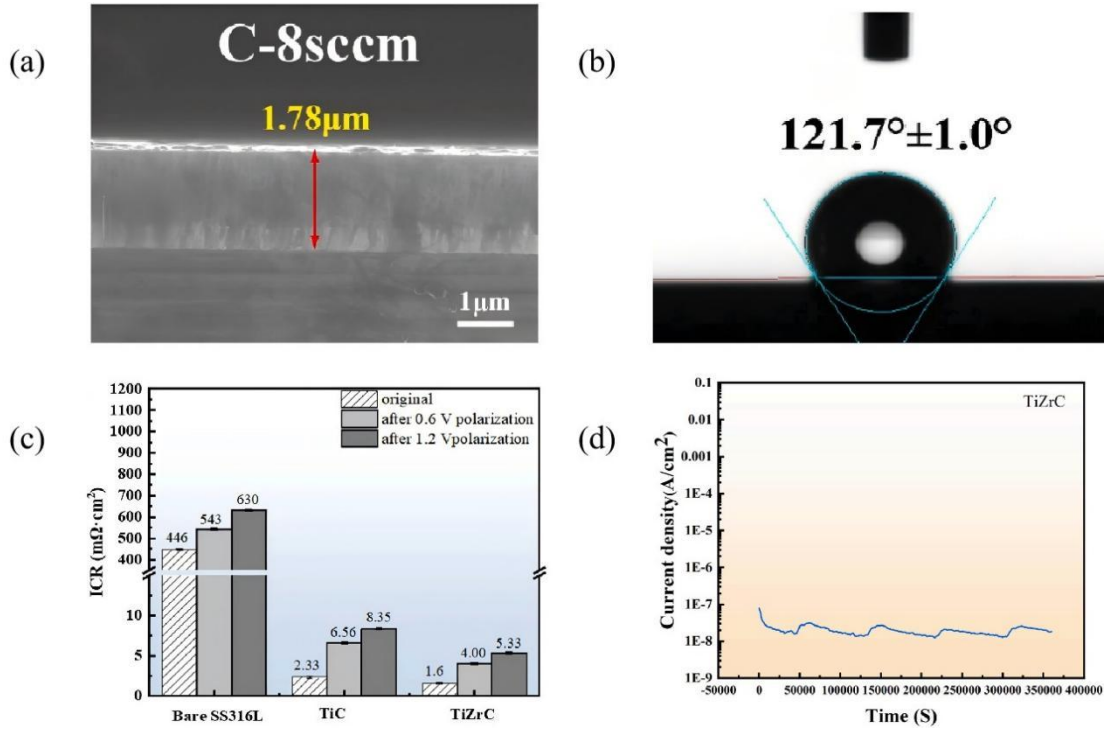

Figure 9. (a) The FE-SEM pictures of the cross-sectional morphology of C-8sccm coatings; (b) The water contact angle of C-8sccm coating samples surface [25]; (c) ICR values of potentiostatic polarization at 1.4MPa; (d) Electrochemical polarization curves of SS316L with TiZrC coating [26].

Chien-Ju Hung et al. Investigated the effects of compression, deformation, and contact area on the Membrane Electrode Assembly (MEA) [27]. It was found that optimal clamping pressure is required for bipolar plates and MEA to achieve the best property of the fuel cell. Insufficient pressure leads to high contact resistance, and excessive pressure reduces the porosity of the Gas Diffusion Layer (GDL), thereby reducing the cell's gas diffusion ability and, consequently, the current density, as shown in Fig. 10(a). At the same time, the contact surface of the bipolar plate with a fillet radius does not have

obvious voids, and the contact is flatter and tighter, reducing the contact resistance. Finally, the corner radius of 0.7 mm and the compression ratio of 46% can be achieved under the conditions of the smallest contact resistance, as shown in Fig. 10(b). Ye Li et al. employed a hybrid flow field design, combining parallel and serpentine flow channels, through the roll forming process, to produce a trapezoidal cross-section for the flow channel [28]. As shown in Fig. 10(c), this design enhances drainage stability and improves hydrogen utilization. The trapezoidal cross-section facilitates air flow to provide sufficient reactants for the cathode and cooling for this cell. The output power is stabilized at 299.4 W and an inlet pressure of 0.6 MPa. After 50 hours, a power density of 311.8 mW/cm is achieved, as shown in Fig. 10(d), indicating that the design can operate stably.

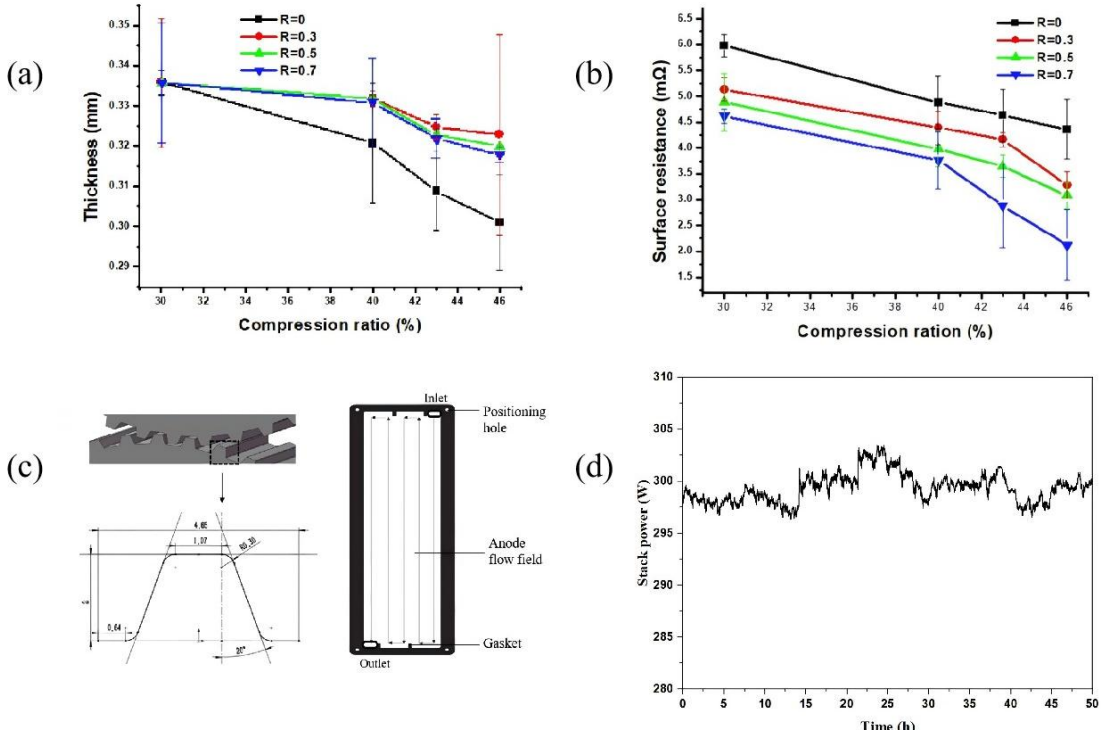

Figure 10. (a) Influence of fillet radius and compression ratio on the thickness of MEA; (b) Effects of fillet radius and compressibility on resistance; (c) Design of the bipolar plate structure and rolling process [27]; (d) Output power curve for 50 h under 30 A load [28].

Bipolar plates in PEMFC can be optimized through structural design and surface treatments. For structural design, appropriate flow field channels can optimize the distribution of gas and water, significantly increasing power density and current density while enhancing water management efficiency. Novel structural designs reduce reactant consumption, extend operating life, and lower electrolysis voltage. Coatings, like CrAlCN and TiZrC can improve corrosion resistance and electrical conductivity through magnetron sputtering and other processes. The productions of bipolar plates with new structures, materials, and coatings require the exploration of low-cost alternative materials, as well as the optimization of the manufacturing process to improve economics.

4. Conclusion

This study significantly improves the overall performance of PEMFCs through the design of non-platinum catalyst active sites and the synergistic optimisation of bipolar plate flow fields. High-density active centres in catalysts can be constructed based on atomically dispersed Fe-N-C sites, combined with sulphur/selenium doping and porous carbon carriers, achieving a half-wave potential of 0.78-0.92 V for the oxygen reduction reaction, a peak power density of up to 890 mW/cm², an H_2O_2 yield of <4%, and durability exceeding 10,000 cycles. The square baffle channel and symmetrical serpentine flow field design in bipolar plate optimisation can increase power density by

12.1–77.88%. The metal foam structure reduces reactant consumption by 22.6%, and the CrAlCN/TiZrC coating technology reduces interfacial contact resistance to 1.60 $m\Omega \cdot cm^2$ and achieves a corrosion current density of 1.344×10^{-8} $A \cdot cm^{-2}$, with a water contact angle of 121.7°±1.0°. Research has confirmed that the regulation of catalyst electronic states and the synergistic interaction between mass transfer and electrical conductivity in bipolar plates are important to overcoming performance bottlenecks.

References

[1] P. Wang, X. Chen, Q. Zhou, Configuration optimization for flow field of PEM fuel cells inspired by the fluid-directed properties of the feather of the bow and arrow, Fuel 404 (2026) 136394.

[2] S. Liu, C. Zhao, J. Li, N. Li, Z. Hu, S. Chen, Excellent proton transfer in proton exchange membrane at low humidity accelerated by sulfonated polyhedral oligosilsesquioxane, Renewable Energy 256 (2026) 123982.

[3] A. Rezaei, M. Rahimi-Esbo, K.D. Firouzjaei, E. Alizadeh, Experimental and numerical investigation on the oxygen distribution in the cathode section of a PEMFC stack, Renewable Energy 256 (2026) 123996.

[4] Y. Yu, Q. Yu, R. Luo, S. Chen, J. Yang, F. Yan, Study on the relationship between lifetime and flow channel in proton exchange membrane fuel cells, Renewable Energy 256 (2026) 124057.

[5] M.H. Elfar, M. Fawzi, A.S. Serry, M. Elsakka, M. Elgamal, A. Refaat, Optimal parameters identification for PEMFC using autonomous groups particle swarm optimization algorithm, International Journal of Hydrogen Energy 69 (2024) 1113-1128.

[6] C.K.T. Weatherly, H. Ren, M.A. Edwards, L. Wang, H.S. White, Coupled Electron- and Phase-Transfer Reactions at a Three-Phase Interface, JOURNAL OF THE AMERICAN CHEMICAL SOCIETY 141 (45) (2019) 18091-18098.

[7] L.C. Xia, M. Ni, Y.W. Dai, K.Q. Zheng, M.X. Li, Numerical study of triple-phase boundary length in high-temperature proton exchange membrane fuel cell, INTERNATIONAL JOURNAL OF ENERGY RESEARCH 46 (2) (2022) 1998-2010.

[8] Z.Z. Du, J. Wang, J. Wang, F. Yu, J.L. Li, X.D. Wang, Research progress of key materials in proton exchange membrane fuel cell br, CAILIAO GONGCHENG-JOURNAL OF MATERIALS ENGINEERING 50 (12) (2022) 35-50.

[9] G.B. Zhang, Z.G. Qu, W.Q. Tao, Y.T. Mu, K. Jiao, H. Xu, Y. Wang, Advancing next-generation proton-exchange membrane fuel cell in multi transfer, JOULE 8 (2) (2024) 45-63.

[10] Y. Nie, Z. Shi, B.W. Li, Q. Meyer, C. Zhao, Engineering Platinum-Based Alloy Catalysts for Oxygen Reduction Reaction in Hydrogen Fuel Cells: A Mini-Review, ENERGY & FUELS 39 (34) (2025) 16049-16064.

[11] P. Lin, J. Sun, C. He, M. Wu, T. Zhao, Modeling proton exchange membrane fuel cells with platinum-group-metal-free catalysts, APPLIED ENERGY 360 (2024).

[12] L. Du, G.X. Zhang, S.H. Sun, Proton Exchange Membrane (PEM) Fuel Cells with Platinum Group Metal (PGM)-Free Cathode, AUTOMOTIVE INNOVATION 4 (2) (2021) 131-143.

[13] D.D. Sun, Z. Wang, M. Jin, J.F. Liu, X. Zhang, S.B. Zhang, H.M. Zhang, Optimizing Ionomer Coverage in Solid Carbon-Supported Catalyst toward High Performance for Proton Exchange Membrane Fuel Cells, ACS APPLIED ENERGY MATERIALS 7 (9) (2024) 4132-4140.

[14] C.Y. Zhu, Y.J. Xing, Effect of High Potential on Carbon Corrosion of Cathode Catalyst Layer in Proton Exchange Membrane Fuel Cells, JOURNAL OF THE ELECTROCHEMICAL SOCIETY 172 (3) (2025).

[15] P. Sun, K. Qiao, D. Li, X. Liu, H. Liu, L. Yang, H. Xu, Z. Zhuang, Y. Yan, D. Cao, Designing oxygen-doped Fe-N-C oxygen reduction catalysts for proton- and anion-exchange-membrane fuel cells, Chem Catalysis 2 (10) (2022) 2750-2763.

[16] J. Cui, J. Min, H. Wang, J. Shui, L. Peng, Z. Kang, J. Liu, Q. Chen, S. Bai, Y. Liu, Elongated Fe–N–C containing trace atomic Co dopants for high power density PEMFCs, Industrial Chemistry & Materials 2 (4) (2024) 634-643.

[17] S. Akula, M. Mooste, B. Zulevi, S. McKinney, A. Kikas, H.-M. Piirsoo, M. Rähn, A. Tamm, V. Kisand, A. Serov, Mesoporous textured Fe-NC electrocatalysts as highly efficient cathodes for proton exchange membrane fuel cells, Journal of Power Sources 520 (2022) 230819.

[18] J. Tao, X. Wang, M. Xu, C. Liu, J. Ge, W. Xing, Non-noble metals as activity sites for ORR catalysts in proton exchange membrane fuel cells (PEMFCs), Industrial Chemistry & Materials 1 (3) (2023) 388-409.

[19] W. Kiciński, S. Dyjak, M. Gratzke, W. Tokarz, A. Błachowski, Platinum group metal-free Fe−N−C catalysts for PEM fuel cells derived from nitrogen and sulfur doped synthetic polymers, Fuel 328 (2022).

[20] J. Baek, H. Son, S.W. Joo, M. Kim, G. Lee, Bimetallic zeolitic imidazole framework-derived sulfur-doped porous carbon as highly efficient catalysts for oxygen reduction reaction in proton exchange membrane fuel cells, Applied Surface Science 642 (2024).

[21] T. Wilberforce, A.G. Olabi, D. Monopoli, M. Dassisti, E.T. Sayed, M.A. Abdelkareem, Design optimization of proton exchange membrane fuel cell bipolar plate, Energy Conversion and Management 277 (2023).

[22] Y. Wei, L. Xu, Y. Li, J. Tan, Better Electrochemical Performance of PEMFC with a Symmetrical Serpentine Flow Field Bipolar Plate, International Journal of Electrochemical Science 17 (12) (2022).

[23] T. Wilberforce, O. Ijaodola, A. Baroutaji, E. Ogungbemi, A.G. Olabi, Effect of Bipolar Plate Material on Proton Exchange Membrane Fuel Cell Performance, Energies 15 (5) (2022).

[24] L. Liao, M. Li, Y. Yin, X. Tan, R. Du, Q. Zhong, F. Zeng, Ti-mesh bipolar plate design and optimization for enhanced PEM electrolyzer performance in water splitting, International Journal of Hydrogen Energy 64 (2024) 981-989.

[25] J. Jin, X. Kou, X. Tian, Y. Tao, X. Xu, H. Yang, Y. Mi, Investigation of corrosion protection with conductive chromium-aluminum carbonitride coating on metallic bipolar plates, Vacuum 213 (2023).

[26] T. Ma, H. Guo, Y. Tian, J. Qi, N. Yao, TiZrC-coated 316 L stainless steel bipolar plates for proton exchange membrane fuel cells, Materials Today Communications 42 (2025).

[27] C.-J. Hung, W.-J. Chen, C.-A. Lin, H.-R. Shiu, B.-H. Chen, Effect of Metallic Bipolar Plates Fillet Radii on Fuel Cell Performance, Energies 14 (21) (2021).

[28] Y. Li, Y. Liu, Q. Liang, L. Han, N. Wan, Z. Guo, Design and performance evaluation of an air-cooled PEMFC stack with metallic bipolar plates, International Journal of Hydrogen Energy 60 (2024) 324-332.